







Magnetism of Ir⁵⁺-based double perovskites: Unraveling its nature and the influence of structureM. A. Laguna-Marco ^{1,2,*}, E. Arias-Egido ^{1,2}, C. Piquer,^{1,2} V. Cuartero,^{3,4} L. Hernández-López ^{1,2}, P. Kayser ⁵,
J. A. Alonso ⁵, J. A. T. Barker,⁶ G. Fabbri ⁷, C. A. Escanhoela Jr.,^{7,8} and T. Irifune^{9,10}¹*Instituto de Ciencia de Materiales de Aragón, CSIC–Universidad de Zaragoza, Zaragoza 50009, Spain*²*Departamento de Física de la Materia Condensada, Universidad de Zaragoza, Zaragoza 50009, Spain*³*European Radiation Synchrotron Facility, 38043 Grenoble, France*⁴*Centro Universitario de la Defensa de Zaragoza, Ctra. Huesca s/n, 50090 Zaragoza, Spain*⁵*Instituto de Ciencia de Materiales de Madrid, CSIC, Cantoblanco, 28049 Madrid, Spain*⁶*Laboratory for Muon-Spin Spectroscopy, Paul Scherrer Institut, CH-5232 Villigen PSI, Switzerland*⁷*Advanced Photon Source, Argonne National Laboratory, Argonne, Illinois 60439, USA*⁸*Centro de Ciências Naturais e Humanas, Universidade Federal do ABC, Santo André, Brazil*⁹*Ehime University, 2–5 Bunkyo-cho, Matsuyama 790-8577, Japan*¹⁰*Earth-Life Science Institute, Tokyo Institute of Technology, Tokyo 152-8500, Japan*

(Received 17 September 2019; published 30 January 2020)

A combination of x-ray-diffraction, x-ray absorption, x-ray magnetic circular dichroism, macroscopic magnetization, and muon-spin relaxation measurements is used to investigate the interplay between structure (both crystallography and microstructure) and magnetism in Sr₂YIrO₆ as a function of both chemical (Ca-doping) and physical (hydrostatic) pressure. X-ray absorption spectroscopy clearly shows that the physical pressure is more effective in modifying the structure. On the other hand, the dichroic measurements evidence a constant magnetic signal with physical pressure and strong differences with Ca-doping. Muon-spin relaxation reveals the presence of magnetic order, even when this is hidden in the magnetization data. From the combined analysis, the magnetic results are explained in terms of the presence of Ir⁶⁺ or Ir⁴⁺ ions in magnetic clusters, most likely located at and triggered by antisite disorder. The measurements under high physical pressure indicate that the magnetic state is independent of the crystallographic details such as Ir-O distances and Ir-O-Y angles.

DOI: [10.1103/PhysRevB.101.014449](https://doi.org/10.1103/PhysRevB.101.014449)**I. INTRODUCTION**

In the past decade, the discovery of new spin-orbit-related phenomena has led to increasing interest in materials containing Ir [1–8]. However, little work has focused on the iridates having pentavalent Ir⁵⁺ ions (5*d*⁴ electronic configuration) as they are expected to be in a Van Vleck nonmagnetic state in the atomic limit, in both the weakly and the strongly interacting regimes. In the strong spin-orbit coupling (SOC) regime, the *J* = 0 state on pentavalent Ir⁵⁺ ions arises from the splitting of the *t*_{2*g*} shell: the lower *j* = 3/2 subshell is fully filled by the four electrons while the upper *j* = 1/2 subshell remains empty. In the Coulomb dominated regime, the first two Hund's rules require each Ir⁵⁺ ion to be in a total *S* = 1 and total *L* = 1 oppositely aligned to *S*, yielding a *J* = 0 state. Recently, however, several experimental counterexamples are casting into doubt this notion. Ca₂RuO₄ (with Ru *d*⁴ electronic configuration) is found to display a moment of 1.3μ_B [9], and double-perovskite iridate Sr₂YIrO₆ (SYIO) has been reported to show well-formed magnetic moments at Ir sites (μ_{eff} = 0.91μ_B/Ir) that order below 1.3 K (*T*_N = 1.3 K, θ_{CW} = −229 K) [10]. This work on SYIO suggested that small structural distortions have the potential to leverage large changes in magnetic behavior (from *J* = 0 to a significant

magnetic moment that can be ordered). This has not only basic scientific interest but also undoubted practical potential in spintronics. Consequently, interest in 5*d*⁴ magnetism has been boosted following this publication [11–19].

From the experimental point of view, several compounds of the Sr_{2−*x*}Ba_{*x*}YIrO₆ series have been revisited in the past four years, but controversial and contradictory magnetic behavior has been reported. Terzic *et al.* reported long-range magnetic order at temperatures below 2 K for several compounds in the Sr_{2−*x*}Ba_{*x*}YIrO₆ series [11]. Ranjbar *et al.* and Phelan *et al.*, by contrast, did not observe any signature for long-range magnetic order in polycrystalline Sr_{2−*x*}Ba_{*x*}YIrO₆ samples [12,13], but they did not investigate properties below 2 K. Corredor *et al.* and Dey *et al.* studied the Sr₂YIrO₆ and Ba₂YIrO₆ (BYIO) compounds, respectively, and concluded that although long-range magnetic order is absent, correlated magnetic moments (0.2–0.5μ_B/Ir) are present [14,15].

Several explanations have been proposed to explain the observed magnetism in Ir⁵⁺ systems. Initially, it was argued that the root cause for the quenching of the *J* = 0 state was the distortion of the IrO₆ octahedra. In particular, the noncubic crystal field created by the distortion would give rise to the partial quenching of the orbital angular momentum [10]. However, studies on Sr_{2−*x*}Ba_{*x*}YIrO₆, where the distortion is gradually decreased down to a perfect cubic situation in Ba₂YIrO₆, found that the moment shows little dependence on the chemical pressure [12,14,15]. This suggests that

*anlaguna@unizar.es

distortions of the octahedra are not responsible for the magnetic moment formation. Theoretical works on the effects of noncubic distortion also report uncertain results. Bhowal *et al.* found that the splitting between the levels due to the noncubic distortion in SYIO is too small, ~ 10 meV, to be responsible for the breakdown of the $J = 0$ state [20]. By contrast, it has been reported that the trigonal distortion in $\text{Sr}_2\text{GdIrO}_6$ gives rise to a splitting of ~ 0.1 eV, one order of magnitude larger than that found for SYIO [20]. Therefore, distortions of the IrO_6 octahedra should still be considered as a possible factor affecting the magnetic state. In relation to the distortion of the IrO_6 octahedra, it should also be noticed that, in addition to chemical substitution, the presence of antisite disorder could also lead to significant local lattice distortions, which can partially quench the orbital angular momentum, thus restoring the magnetic moment [21].

Several experimental groups have proposed that the magnetism observed in their $\text{Sr}_{2-x}\text{Ba}_x\text{YIrO}_6$ samples is ascribed to Ir^{6+} and/or Ir^{4+} paramagnetic impurities (estimated to be $< 5\%$ in all cases) [12–16,18] caused by chemical disorder and/or off-stoichiometry. While the presence of Ir^{6+} and/or Ir^{4+} impurities cannot be *a priori* ruled out, identifying them as the origin of magnetic correlations is not without controversy.

Alternatively, magnetism in d^4 -based oxides has been proposed to arise from condensation of $J = 1$ triplon excitations [22,23]. In this scenario, if the energy of the $J = 1$ state is sufficiently small, the interatomic exchange due to electron hopping may lead to the onset of (anti)ferromagnetism. Regarding the works that focused on iridates, Bhowal *et al.* studied through first-principles calculations the electronic structure of double-perovskite iridates with Ir^{5+} and found a finite moment at the Ir site that was attributed to a band-structure effect [20]. Later calculations, however, called into question the breakdown of the $J = 0$ state in double-perovskite iridates as they found that Ir-Ir hopping is too small to give rise to bandwidths that can overcome the singlet-triplet gap of ~ 200 meV [24,25]. Density-functional theory (DFT) calculations by Chen *et al.* [26] also suggest that magnetic condensation is unlikely in perfect SYIO and BYIO systems. However, they also suggest that Y/Ir intersite disorder can induce magnetism ($J = 1$ triplon) inside the intersite disordered clusters because of enhanced interactions due to increased orbital overlap and an increased number of orbitals mediating the interactions. It should be noticed, therefore, that there are two mechanisms that could possibly link antisite disorder and the formation of magnetic moments, namely via distortions or via triplon condensation.

There are other possible mechanisms that could contribute to stabilize a magnetic moment in pentavalent Ir systems: a volume contraction would result in an increment of the hybridization, which could not only reduce the orbital angular momentum but also increase the electron hopping and the bandwidth of the $5d$ subshells. Taking into account the extended nature of the $5d$ orbitals, it cannot be discarded beforehand that this structural modification changes the delicate balance between interactions present in these systems, destabilizing the $J = 0$ state. Doping is an alternative mechanism. Chaloupka *et al.* have carried out a theoretical study of the effect of light doping with d^5 ions ($J = 1/2$ states, assuming

strong SOC), and they found that the interaction between J excitons and doped carriers may convert the nonmagnetic and insulating parent into a ferromagnetic metal [27].

From the above scenario, it is inferred that the key questions remain unsolved: What are the root causes of the magnetism in these $5d^4$ compounds? Can $5d^4$ iridates become magnetic through structural (lattice contraction, distortions, defects, etc.) modification? Our work aims to provide insight into both questions. Regarding the origin of the magnetism, we present, in addition to bulk magnetometry, results from muon-spin relaxation and x-ray magnetic circular dichroism (XMCD) measurements to get further insight and better identify the origin of the magnetic behavior. Regarding the link between structure and magnetism, it is to be expected that both the crystal field and the hopping will become more important factors in determining the electronic structure of these compounds as the lattice volume is reduced. For this purpose, we have tracked the changes in the net magnetic moment per Ir as the lattice volume decreases from the initial SYIO by applying both chemical (newly synthesized Ca-doped $\text{Sr}_{2-x}\text{Ca}_x\text{YIrO}_6$) and physical pressure. We explore whether the volume contraction or the structural distortions cause any change in the magnetic response.

II. EXPERIMENT

Polycrystalline samples of $\text{Sr}_{2-x}\text{Ca}_x\text{YIrO}_6$ were prepared by solid-state reaction. The appropriate stoichiometric mixture of SrCO_3 (Aldrich, 99.99%), CaCO_3 (Aldrich, 99.99%), Y_2O_3 (Aldrich, 99.999%), and Ir metal (Aithaca, 99.9%) was weighed and finely mixed by hand in an agate mortar. Prior to weighing the reagents, CaCO_3 and SrCO_3 were dried at 150°C for 12 h and Y_2O_3 was heated at 1000°C for 12 h. The samples were placed in alumina crucibles and heated at 650°C for 12 h and 850°C for 12 h with intermediate regrinding. After mixing again, the samples were pressed into 20 mm pellets and heated in air at 1050°C for 24 h, 1200°C for 72 h, and 1400°C for 72 h.

Synchrotron x-ray diffraction (SXRD) experiments were carried out in transmission mode on the BL04-MSPD beamline [28] of the ALBA synchrotron (Barcelona, Spain) using the highest angular resolution mode as provided by the multi-analyzer detector (MAD) setup. Fine powder was sealed in 0.7-mm-diam quartz capillaries. Data were collected while rotating the sample to increase powder averaging. The beam energy was 38 keV ($\lambda = 0.32511 \text{ \AA}$), selected to optimize absorption. Temperature-dependent SXRD patterns were collected at 25°C for $\text{Sr}_{2-x}\text{Ca}_x\text{YIrO}_6$ ($x = 0, 0.2, 0.4,$ and 0.6), and then at $200, 400, 600,$ and 800°C for the $x = 0$ sample. The diffraction patterns were Rietveld-refined using the FULLPROF code [29].

The extended x-ray absorption fine structure (EXAFS) spectra at the Ir L_3 absorption edge were recorded at ambient pressure and room temperature (RT) as well as under applied high pressures (from 2.5 GPa up to 43 GPa) and low temperature ($T = 10 \text{ K}$) at the BM23 [30] and ID24 [31] beamlines of the ESRF (Grenoble, France), respectively. In the first case the incoming energy was selected by using a Si (111) double-crystal monochromator, and higher-order

harmonics were rejected by a Si mirror set at 2.2 mrad. Measurements were performed in transmission using ionization chambers. An ID24 energy-dispersive spectrometer was used to perform the low-temperature and high-pressure x-ray absorption spectroscopy (XAS) measurements. The measurements were also performed in transmission by using a one-dimensional Hamamatsu CCD camera. We used nanopolycrystalline diamond anvils [32] to avoid glitches from the anvils on the EXAFS spectra and a He-flow cryostat. Ruby chips were used as pressure markers and Ne gas was used as a pressure-transmitting medium. The EXAFS spectra were analyzed according to standard procedures [33] using the HORAE-IFEFFIT (Athena, Artemis) program package [34,35]. For the analysis of the EXAFS spectra at the Ir L_3 edge, a cluster 7 Å in size was used in calculating theoretical standards.

The magnetic properties were studied with a commercial superconducting quantum interference device (SQUID) magnetometer from Quantum Design. The magnetic susceptibility was measured both in zero-field-cooled (ZFC) mode and field-cooled (FC) mode in the $5 \leq T \leq 300$ K range under an applied magnetic field of 1000 Oe. Isothermal magnetization curves were obtained for magnetic fields in the -50 to 50 kOe range at 5 and 1.8 K.

Muon-spin relaxation (μ SR) experiments were carried out using the GPS instrument at the Swiss Muon Source, Paul Scherrer Institute, Villigen, Switzerland. Spin-polarized positive muons (+, mean lifetime 2.2 s, momentum 28 MeV/c) were implanted into the powdered sample. The time evolution of the muon-spin polarization [the asymmetry function, $A(t)$] is calculated by counting emitted decay positrons forward (f) and backward (b) of the initial muon-spin direction with scintillation counters. The asymmetry measurements were performed in the temperature range between 5 and 300 K and in a zero-field configuration. Two additional measurements with applied 50 G transverse field were performed to get the value of α (experimental calibration constant) and the volume fractions.

The XANES/XMCD measurements under high pressure were carried out at beamline 4-ID-D of the Advanced Photon Source, Argonne National Laboratory. The spectra were recorded at the Ir $L_{2,3}$ absorption edges ($2p_{\frac{1}{2},\frac{3}{2}} \rightarrow 5d$ transition) to probe the Ir $5d$ states. Circularly polarized x rays were generated using phase-retarding optics [36,37]. Harmonic rejection was achieved by the combined effects of x-ray reflection from two Pd mirrors at a 3.1 mrad incidence angle and detuning of the second crystal in the Si(111) double-crystal monochromator. XMCD was measured by switching x-ray helicity (13.1 Hz) and detecting the related modulation in absorption coefficient with a lock-in amplifier [38]. All the measurements were done in transmission geometry, at low temperature (10 K) and under a magnetic field of 3.5 T applied along the x-ray propagation direction. For the high-pressure measurements, the powdered samples were loaded on copper-beryllium diamond anvil cells (DACs) fitted with 300- μ m culet anvils and a Re gasket [39]. Ne gas was used as the quasi-hydrostatic pressure transmitting medium and ruby spheres for *in situ* pressure calibration. Low temperature was reached using a He-flow cryostat, and pressure was controlled remotely using a He-gas membrane.

TABLE I. Summary of the main structural parameters of the $\text{Sr}_{2-x}\text{Ca}_x\text{YIrO}_6$ samples measured at room temperature: cell parameters, averaged Ir-O-Y bond angle (φ), and IrO_6 octahedra distortion parameter $\{\Delta_d = (1/6) \sum_{n=1,6} [(d_n - \langle d \rangle) / \langle d \rangle]^2\}$.

x	a (Å)	b (Å)	c (Å)	β (deg)	φ (deg)	$\Delta_d \times 10^{-4}$
0	5.78438(4)	5.79585(5)	8.18411(7)	90.2468(4)	158.2	0.37
0.2	5.7677(1)	5.7950(1)	8.1709(1)	90.268(1)	159.4	2.4
0.4	5.7601(2)	5.7781(2)	8.1617(2)	90.447(1)	156.6	6.6
0.6	5.7542(2)	5.7713(2)	8.1520(3)	90.510(2)	153.7	16.0

III. STRUCTURAL CHARACTERIZATION

A. Chemical pressure

For all the $\text{Sr}_{2-x}\text{Ca}_x\text{YIrO}_6$ samples, where x indicates nominal compositions, the structure at RT is described in a monoclinic unit cell, $P2_1/n$ space group (no. 14), and the main parameters are summarized in Table I (see the Supplemental Material for details [40]). As expected, the substitution of Sr^{2+} ions by smaller Ca^{2+} ions causes a small, monotonic decrease in the three lattice parameters. This reduction, however, is not the same in the three directions. For $x = 0.6$, a 0.51%, 0.41%, and 0.38% reduction is obtained for the a , b , and c parameters, respectively. In addition, the β angle increases. This implies a slightly increasing distortion in the crystal structure, as expected from the concomitant reduction of the tolerance factor upon introducing a smaller ion. As shown in Table I, according to the x-ray diffraction (XRD) data, not only does the structural distortion increase because of the increment of the octahedral tilting (i.e., reduction of the Ir-O-Y bond angle), but also the octahedron itself becomes more distorted upon Ca introduction.

Additionally, the Y/Ir antisite has been explored in the four samples, finding that it is small ($<1\%$) in all the cases. For $x = 0$, we have $0.6 \pm 0.2\%$ of the Ir sites occupied by Y. Regarding the effect of doping, no monotonic evolution is found as a function of doping. On the other hand, as the doping level of Ca increases, a part of it is incorporated at the octahedral sublattice instead of Y: 4.2% Ca at Y sites is found for the $x = 0.2$ compound and 11% for the $x = 0.4$ and 0.6 compounds. This favors the formation of disordered regions and implies that Ir is partially oxidized to Ir^{6+} .

At first glance, the EXAFS spectra show no substantial changes with Ca-doping (see Fig. 1). To correlate the spectral features with specific structural or compositional changes, we take advantage of the Fourier transform (FT), which provides a measure of the radial distribution function around the Ir atom. In addition, taking as a starting point the SYIO crystal structure [13], we have considered a simplified model that includes the contributions to the EXAFS signal coming from four single scattering (SS) paths up to 6 Å (that is, O, Sr/Ca, Y, and Ir coordination shells around the absorbing Ir) as well as the (quasi)collinear, focusing multiple scattering (MS) paths involving the same atoms from which the SS occurs (i.e., O-Ir_{abs}-O, Y-O, and O-Y-O scattering paths). Each coordination shell has one unique average distance (R_j) and one Debye-Waller (DW) factor. The R_j lengths and DW factors of the

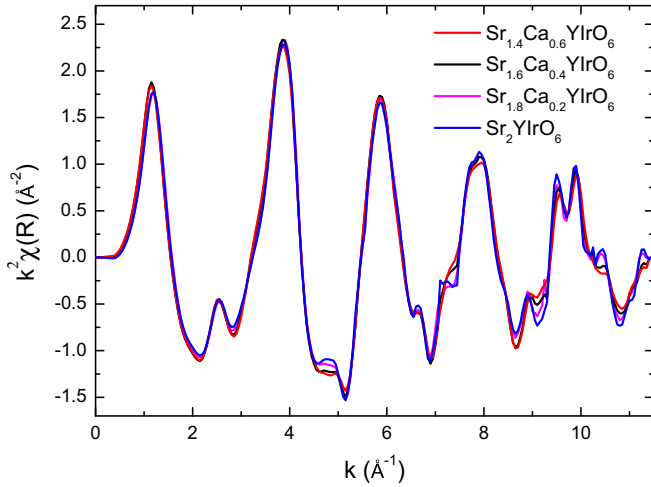


FIG. 1. k^2 -weighted Ir L_3 -edge EXAFS signals recorded at RT in the transmission mode.

MS paths are parametrized in terms of the SS paths in a similar manner to that described in Refs. [41,42], but the Ir-O-Y angle in our case remains fixed to that derived from the crystal structure refinement. Other models dividing the coordination shells into several *subshells* (thus increasing the number of SS paths) were tested but gave worse fitting parameters. The best-fit values are summarized in Table II for the end members of the series. Comparison of the two panels in Fig. 2 clearly shows that the evolution with Ca [panel (a)] is very well reproduced in the fits [panel (b)].

The first peak on the FT curve corresponds to the first coordination shell around Ir, that is, the octahedral IrO_6 environment. As can be seen in the FT represented in Fig. 2(a), no shift is observed in the first peak, indicating no measurable modification of the average Ir-O distance. The intensity shows only very small differences (whose trend is in agreement with the distortion parameter obtained by XRD), and the width of the peak remains constant. This indicates that the distortion

TABLE II. Values of the best-fit structural parameters: half path lengths/interatomic distances [R_j , in (Å)] and Debye-Waller factors [σ^2 , in (Å²)] for the $\text{Sr}_{2-x}\text{Ca}_x\text{YrO}_6$ samples. The number of atoms at mean distances R_j around the absorbing atom (N_j) is fixed in the model. $S_0^2 = 0.89$ and ΔE_0 (eV) = 6.23 have been fixed to the values obtained for the SYIO sample measured at ambient pressure. The R -factor, which is a measure of the misfit between the data and theory, is 0.02 for the ambient data and 0.04 for HP data.

	$x = 0$ 0 GPa	$x = 0.6$ 0 GPa	$x = 0$ 2.5 GPa	$x = 0$ 16.2 GPa	$x = 0$ 43.2 GPa
R_1 (Ir-O)	1.937(6)	1.939(7)	1.931(9)	1.908(6)	1.891(4)
R_2 (Ir-Sr)	3.43(5)	3.42(3)	3.43(9)	3.47(7)	3.21(6)
R_3 (Ir-Y)	4.05(5)	3.95(4)	4.00(9)	3.56(3)	4.33(9)
R_4 (Ir-Ir)	5.76(6)	5.75(7)	5.82(10)	5.90(14)	5.86(6)
σ_1^2	0.003(1)	0.003(1)	0.002(1)	0.003(1)	0.005(1)
σ_2^2	0.020(8)	0.017(4)	0.017(13)	0.016(11)	0.029(10)
σ_3^2	0.011(6)	0.009(5)	0.007(10)	0.003(3)	0.014(11)
σ_4^2	0.007(8)	0.010(8)	0.004(12)	0.010(19)	0.006(8)

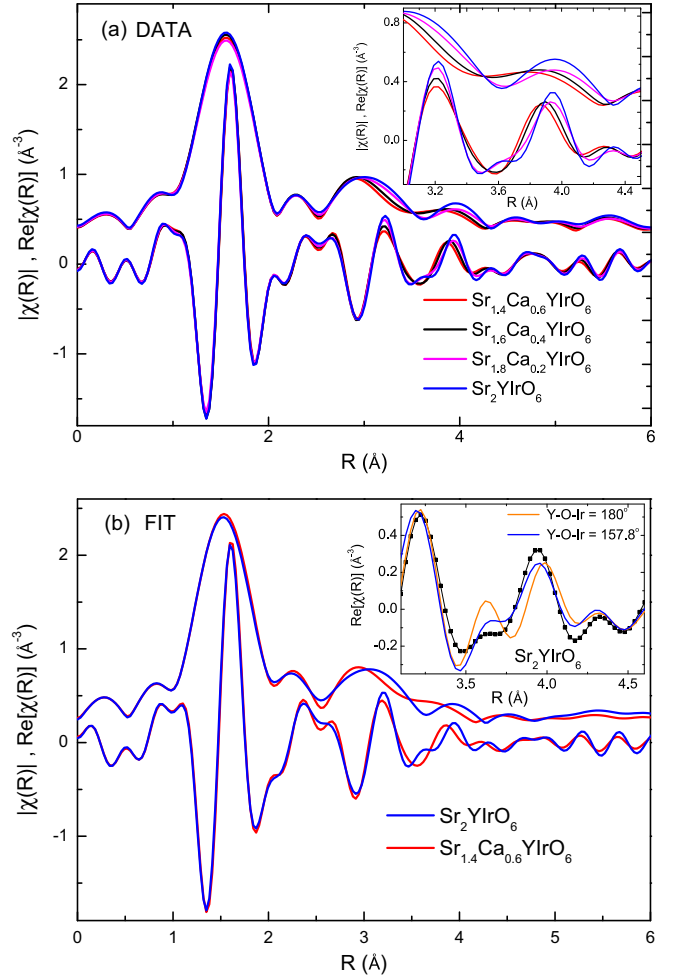


FIG. 2. (a) Modulus and real part of the FTs of the EXAFS signals for the polycrystalline samples (k -range from 2.8 to 9.4 Å⁻¹; k^2 -weighted; R -range from 1.15 to 5.7 Å, Hanning window, $dk = 0.5$ Å⁻¹). Despite the good quality of the data, a short k -range was selected in order to follow a similar analysis for ambient and high-pressure data. The same trends are found when a larger k -range up to 16 Å⁻¹ is used. The inset show a zoomed region. (b) Comparison of the best fits obtained for $x = 0$ and 0.6 samples. In the inset, the effect of changing the Y-O-Ir angle is shown (see the text for details).

of the IrO_6 octahedra does not have any significant variation with Ca-doping. It should be noted, however, that the spatial resolution in our EXAFS is ~ 0.1 Å, so very small distortions could be hidden in our data.

According to our analysis results, the main contribution to the $R \sim 2.2$ – 3.4 Å range comes from the MS O-Ir-O path. The Sr atoms also contribute at this R range, but the intensity of its contribution is small as reflected by the large DW values (Table II). This agrees well with the fact that the structure of SYIO [13] actually presents four different Ir-Sr distances spanned in a broad range. As a consequence, substituting Sr by Ca in the model does not make any noticeable difference. The main contribution to the feature at $R \sim 3.9$ Å is associated with the Y shell (and its concomitant SS and MS paths), and the features at $R \sim 5.6$ Å and $R \sim 7.0$ Å are due to the scattering coming from the Ir atoms.

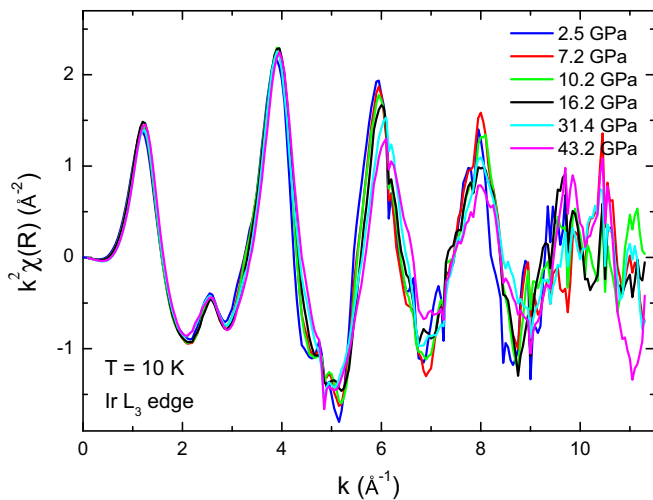


FIG. 3. k^2 -weighted Ir L_3 -edge EXAFS signals recorded on the Sr_2YIrO_6 sample at 10 K in the transmission mode.

As shown in Fig. 2(a), the main spectral modification is located around 3.4–4.2 Å, which noticeably shifts toward lower R . Our analysis of the EXAFS spectra indicates that the differences observed with Ca-doping are not due to the chemical substitution itself but are associated with structural changes related to the Ir-O-Y angle. In particular, the fact that the length of the Y-related scattering paths decreases clearly more than the rest (see Table II) suggests that the main structural change is an increase of the Ir-O-Y tilting. This is in agreement with the evolution of φ found by XRD (Table I). To get further evidence, we have simulated the FT profile assuming a perfectly collinear Y-O-Ir angle. We have fixed all the parameters to those in Table II, but the Y-related MS paths have been modified to be perfectly collinear (and with a total length equal to that in the SS path) and their DW factors have been increased. According to the simulation in the inset of Fig. 2(b), as the angle decreases the feature at $R \sim 3.9$ Å shifts toward lower R . This further supports an increasing tilting of the Ir-O-Y angle with Ca-doping.

B. Physical pressure

In contrast to the Ca-doping case, a gradual evolution of the EXAFS oscillations is observed as the pressure is increased (Fig. 3). This indicates that the application of hydrostatic pressure gives rise to larger changes in the structure than applying chemical pressure. To further analyze the effect of physical pressure on the structure, the same model as for chemical pressure has been used (with the same ranges and parameters). The best-fit values for three representative pressures have been included in Table II, and the fits can be observed in Fig. 4(b).

Regarding the octahedral IrO_6 environment, a shift is observed in the first peak, indicating a reduction of the average Ir-O distance [Fig. 4(a)]. According to our analysis, the average Ir-O distance in the IrO_6 octahedra reduces by 0.05 Å, i.e., a 2.6% reduction. The intensity also tends to decrease with increasing pressure. This is typically indicative of an increasing distortion of the IrO_6 octahedra, but it can also indicate an increasing pressure gradient along the sample.

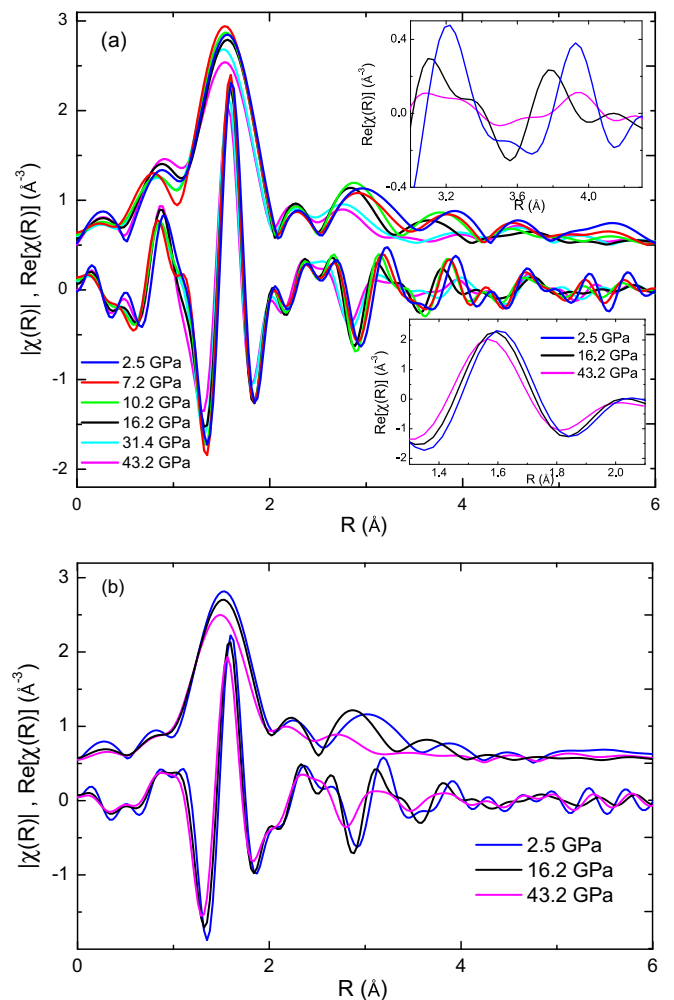


FIG. 4. (a) Modulus and real part of the FTs of the EXAFS signals for the SYIO sample (k -range from 2.8 to 9.4 Å⁻¹; k^2 -weighted; Hanning window, $dk = 0.5$ Å⁻¹). The insets show zoomed regions. (b) Comparison of the best fits obtained for $P = 2.5, 16.2,$ and 43.2 GPa at $T = 10$ K.

The main spectral modification is again located around 3.0–4.2 Å. The feature at $R \sim 3.1$ Å shows a progressive decrease of the intensity and a gradual shift toward lower R up to the higher measured pressure, in accordance with the decrease of the Ir-O distances. Regarding the feature at $R \sim 3.9$ Å, up to 16 GPa there is a clear shift toward lower R that suggests a large increase of the tilting of the Ir-O-Y angle. From 16 to 31 GPa the trend changes. The profile for 31 and 43 GPa may be indicative of either a relaxation of the tilting or simply a very large degree of distortion induced by the highest pressures. In any case, the EXAFS results show that both the Ir-O distance (as shown in Table II) and the Ir-O-Y angle are modified to a greater extent by hydrostatic pressure than by chemical pressure.

IV. MAGNETIC CHARACTERIZATION

A. Ambient pressure

Our measurements on Sr_2YIrO_6 indicate the lack of long-range magnetic order at least to 1.8 K. The magnetization at

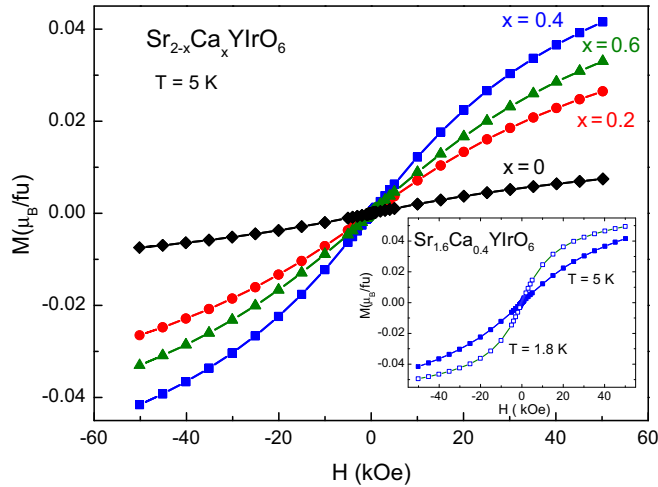


FIG. 5. Magnetization vs applied field curves recorded at $T = 5$ K for $\text{Sr}_{2-x}\text{Ca}_x\text{YrO}_6$ compounds. Inset: magnetization vs applied field curves recorded at $T = 5$ and 1.8 K for $\text{Sr}_{1.6}\text{Ca}_{0.4}\text{YrO}_6$.

$T = 5$ K and $H = 50$ kOe is $0.008\mu_B/\text{f.u.}$ and the effective magnetic moment estimated from the $M(T)$ curves is roughly $\mu_{\text{eff}} \sim 0.3\mu_B/\text{Ir}$. These values are in good agreement with the values previously reported by Phelan *et al.* ($\mu_{\text{eff}} \sim 0.4\mu_B/\text{Ir}$) [12], Ranjbar *et al.* ($\mu_{\text{eff}} \sim 0.16\mu_B/\text{Ir}$) [13], and Corredor *et al.* ($M_{\text{max}} \sim 0.014\mu_B/\text{Ir}$ and $\mu_{\text{eff}} \sim 0.21\mu_B/\text{Ir}$) [15]. Other values reported for $\text{Ba}_{2-x}\text{Sr}_x\text{YrO}_6$ and LaSrBiIrO_6 samples are also in the 0.16 – $0.63\mu_B/\text{Ir}$ range [14,16,26]. On the other hand, Cao *et al.* found higher μ_{eff} ($\mu_{\text{eff}} = 0.91\mu_B/\text{Ir}$) as well as long-range magnetic order below 1.8 K [10,11].

In all those cases in which the magnetic response has been reported to be ascribed to paramagnetic impurities, a small percentage, $\leq 5\%$, has been estimated [13–16,18]. Following these works, the amount of magnetic centers would be $\sim 3\%$ in our Sr_2YrO_6 sample [estimated from μ_{eff} and assuming Ir^{4+} ions, this value is smaller if estimated from $M(H)$ data].

While no data have been reported for the Ca-doped samples so far, our results show that Ca-doping does not induce any magnetic transition or drastic change of the magnetic behavior. As can be seen in Figs. 5 and 6, no evidence of long-range magnetic order is observed down to $T = 1.8$ K. Despite that, the magnetization values at $T = 5$ K and $H = 50$ kOe (Fig. 5) and the effective magnetic moment (Fig. 6) of the doped samples are somewhat larger than those found in our Sr_2YrO_6 sample. $M = 0.043\mu_B/\text{f.u.}$ and $\mu_{\text{eff}} \sim 0.6\mu_B/\text{Ir}$ for $x = 0.4$.

Additionally, it should be noted that the shape of our $M(H)$ and $M(T)$ curves, slightly departing from a perfect canonical paramagnetic behavior, indicates the presence of correlated magnetic moments, in agreement with that found by Dey *et al.* and Corredor *et al.* [14,15].

The XMCD measured on Sr_2YrO_6 consists of a small but clear negative peak at the Ir L_3 edge, while no signal is observed at the L_2 edge. By contrast, the doped sample shows XMCD signals with similar intensity and opposite sign at the Ir L_3 and L_2 edges. Application of sum rules [43,44] results in $m_L \sim 0.0029\mu_B$; $m_S \sim 0.0042\mu_B$ for $x = 0$ and $m_L \sim 0.0006\mu_B$; $m_S \sim 0.0108\mu_B$ for $x = 0.4$ (using

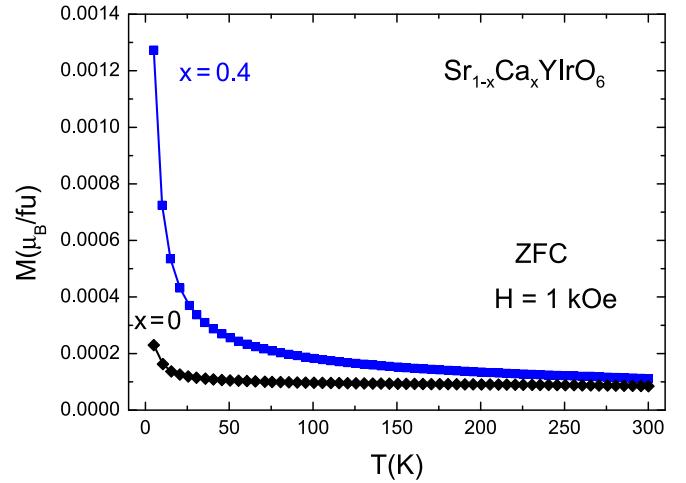


FIG. 6. Magnetization vs temperature recorded with an applied field of 10 kOe after zero-field cooling on $\text{Sr}_{1-x}\text{Ca}_x\text{YrO}_6$ compounds with 0, 0.4, and 0.8 Ca-doping. No difference is observed between ZFC and FC curves (not shown).

$\langle T_z \rangle / \langle S_z \rangle = 0.056$ [45]; if $\langle T_z \rangle = 0$ is used we obtain $m_S \sim 0.0051\mu_B$ and $m_S \sim 0.0130\mu_B$, respectively). While the total magnetic moments obtained from XMCD are slightly different from magnetometry, it confirms an increase of the net magnetization in the doped sample. There is also a drastic quenching of the Ir orbital magnetic moment, with the $\langle m_l \rangle / \langle m_s \rangle$ ratio dropping by more than a factor of 10 from $x = 0$ to 0.4 ($\langle m_l \rangle / \langle m_s \rangle \sim 0.69$ and 0.06, respectively). The XMCD spectra in Fig. 7, therefore, show an unexpectedly different nature of the magnetic moment for $x = 0$ and 0.4 samples.

A simple profile comparison with other spectra corresponding to Ir^{4+} , Ir^{5+} , and Ir^{6+} double-perovskite iridates [46] (the particular case of $\text{Sr}_2\text{ZnIrO}_6$ has been directly included in Fig. 7) allows us to undoubtedly rule out the presence of Ir^{6+} ions in Sr_2YrO_6 while its presence is evidenced in $\text{Sr}_{1.6}\text{Ca}_{0.4}\text{YrO}_6$. Regarding the possible presence of Ir^{4+} ions in Sr_2YrO_6 , the similar profiles of Ir^{4+} and Ir^{5+} XMCD spectra [46] prevent us from straightforwardly discarding the presence of Ir^{4+} ions in the undoped sample. It is worth noticing at this point that Fuchs *et al.* reported a major Ir^{6+} contribution in the nondistorted Ba_2YrO_6 sample [18].

The muon-spin relaxation (μSR) technique is used to study the spin order and dynamics arising from the Ir moment. The muon asymmetry spectra for SYIO in zero applied magnetic field are shown in Fig. 8(a). Unambiguous oscillations are observed for temperatures below 50 K, indicating the presence of magnetic order even when this is not observed in dc magnetization measurements. It should be noted here that the characteristic time windows corresponding to the two techniques are rather different: 10^{-1} – 10^2 s in the case of the SQUID magnetometry and 10^{-5} – 10^{-3} s for μSR .

The time dependence of the muon-spin polarization in Fig. 8(a) is found to be best described by the following two-component functional form:

$$A(t) = A_1 j_0(\gamma B t) e^{-\lambda_1 t} + A_2 e^{-(\lambda_2 t)^\beta},$$

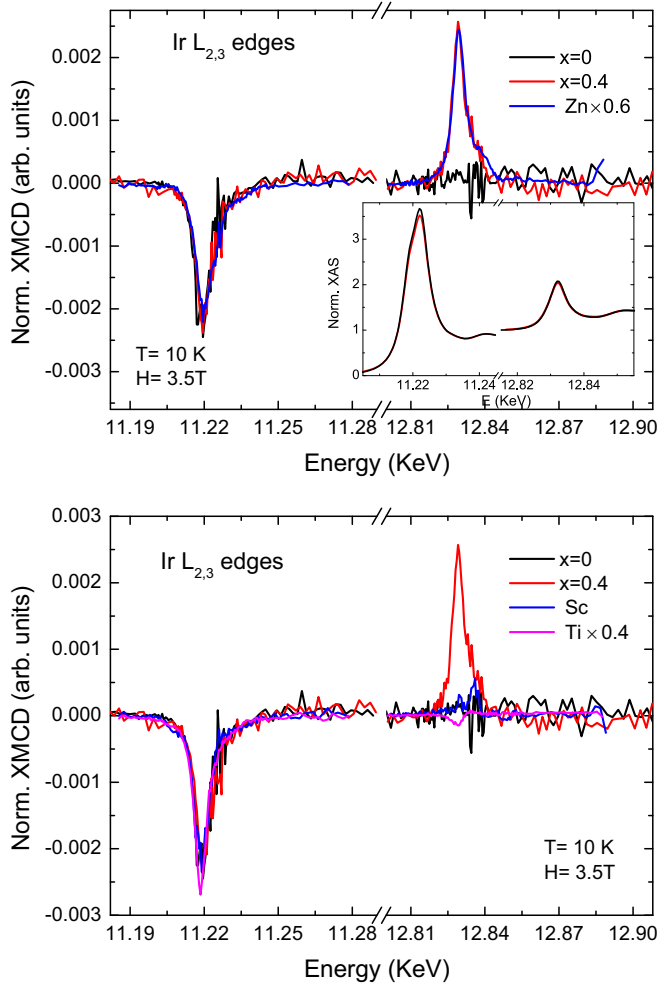


FIG. 7. Top: XMCD spectra recorded at the Ir $L_{2,3}$ edges at ambient pressure on $\text{Sr}_{2-x}\text{Ca}_x\text{YIrO}_6$ samples with $x = 0$ and 0.4 and $\text{Sr}_2\text{ZnIrO}_6$ (Ir^{6+}) samples. Inset: detail of the XAS signal at Ir $L_{2,3}$ edges for $x = 0$ and 0.4 samples. Bottom: XMCD spectra recorded at the Ir $L_{2,3}$ edges on $\text{Sr}_{2-x}\text{Ca}_x\text{YIrO}_6$ samples with $x = 0$ and 0.4 and $\text{Sr}_2\text{ScIrO}_6$ (Ir^{5+}) and $\text{Sr}_2\text{TiIrO}_6$ (Ir^{4+}) samples.

where j_0 is a Bessel function, A_1 and λ_1 are the amplitude and damping rate of the oscillating (magnetic) fraction, and A_2 and λ_2 are the amplitude and relaxation rate of the relaxing (nonmagnetically ordered) fraction. The results of the fit analysis are shown in Fig. 9.

The value of A_1 obtained from the fits, and reflecting the percentage associated with the volume fraction of the magnetically ordered phase, is 15% at low temperature [Fig. 8(b)]. This is in agreement with the percentage obtained by measuring the muon asymmetry under a weak external field H_{ext} . The amplitude of the muon signal precessing under H_{ext} reflects the volume fraction of the sample that is paramagnetic or not ordered magnetically. Therefore, to determine the fraction of magnetic and nonmagnetic phases, the asymmetry at 300 and 5 K under a weak ($H_{\text{ext}} = 50$ Oe) transverse applied field has been measured. From the data in Fig. 8(b), we obtain that the volume fraction of the magnetic phase at $T = 5$ K is 17%. This volume fraction implies that the magnetic signal is not coming from the majority of the Ir^{5+}

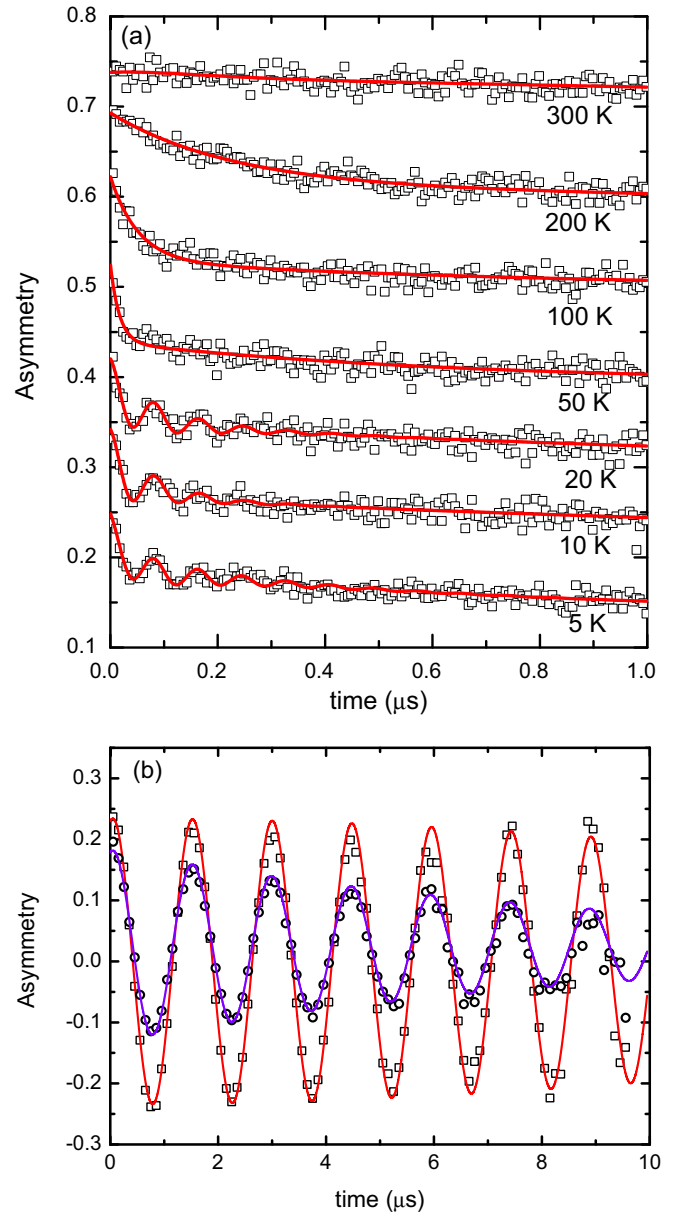


FIG. 8. (a) Time-dependent muon-spin polarization of SYIO in zero external field is shown for selected temperatures for SYIO. The spectra are vertically shifted for the sake of clarity. The solid lines are fits. (b) Muon asymmetry spectra measured on SYIO with an external 50 Oe transversal field at both $T = 5$ and 300 K. The solid lines are fits.

ions. That is to say, the magnetic response is not homogeneous throughout the sample. At the same time, a 17% volume fraction of magnetically ordered phase is in disagreement with a tiny percentage of isolated paramagnetic centers.

As for the magnitude of the local magnetic field at the muon site in SYIO, the value obtained from the fit [Fig. 9(a)] is very close to the 958 Oe reported for $\text{La}_2\text{CuIrO}_6$ [47]. Despite the fact that this Ir^{4+} compound crystallizes in the triclinic $P\bar{1}$ space group, which presents a reduced symmetry relative to the $P2_1/n$, and in spite of the presence of magnetic Cu^{2+} ions ($\mu_{\text{Cu}} = 0.69\mu_B$; $\mu_{\text{Ir}} = 0.45\mu_B$) [47], which does not allow us to assume the same magnetic structure, we can

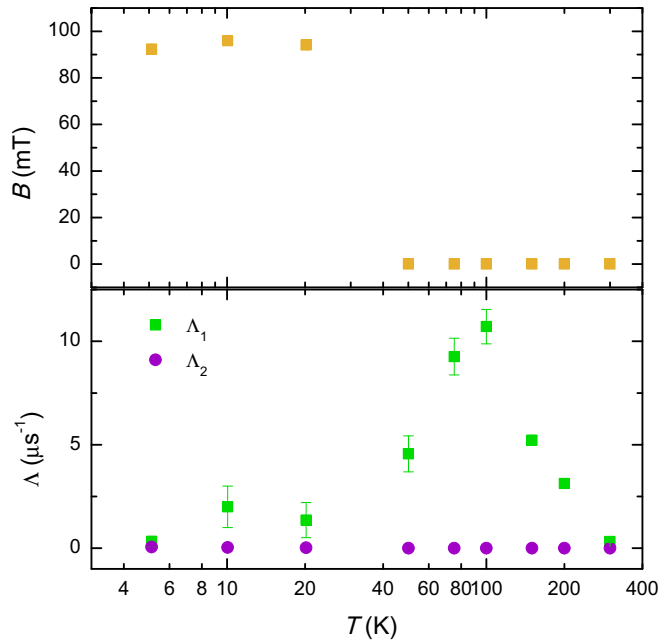


FIG. 9. Temperature dependence of the parameters extracted from zero-field data: (a) magnitude of the magnetic field at the muon site, and (b) muon relaxation and damping rates.

still reasonably assume a similar muon site for both compounds and a similar magnetic moment of the iridium atoms in both compounds, or at least a sizable magnetic moment for the Ir ions in our compound. In addition, a well-defined oscillation frequency indicates the development of one distinct internal magnetic field at the muon site. This seems to rule out the possibilities of a spin-glass state or an incommensurate state, confirming a commensurate magnetic order instead. On the other hand, the fact that the spectra are better fit to a Bessel function could indicate very inhomogeneous behavior across the SYIO sample.

λ_1 accounts for the relaxation of the oscillation and is a measure of the width of the static Gaussian field distribution. Dynamical effects are also present in λ_1 . Interestingly enough, the damping rate peaks at $T = 100$ K [Fig. 9(b)] and not in the $T = 20$ – 50 K range, where the oscillation disappears and one could expect a magnetic transition. The thermal evolution of λ_1 suggests the onset of magnetic correlations or dynamic local order already at 200 K. The change from a slowly relaxing behavior at 300 K to a fast-relaxing behavior at 200 K in Fig. 8(a) also supports this idea.

Overall, the magnetic signal in the μSR data can be better explained as coming from segregated magnetic clusters. In addition, the analysis of these data suggests a sizable Ir magnetic moment and the presence of magnetic correlations (or even well-developed dynamic magnetic order) at temperatures below 200 K.

B. Physical pressure

As shown in Fig. 10, as the pressure increases, the intensity of the x-ray absorption near-edge structure (XANES) signal at the Ir L_3 edge undergoes a slight, gradual decrease ($\sim 0.19\%/GPa$), while at the L_2 edge it remains invariable.

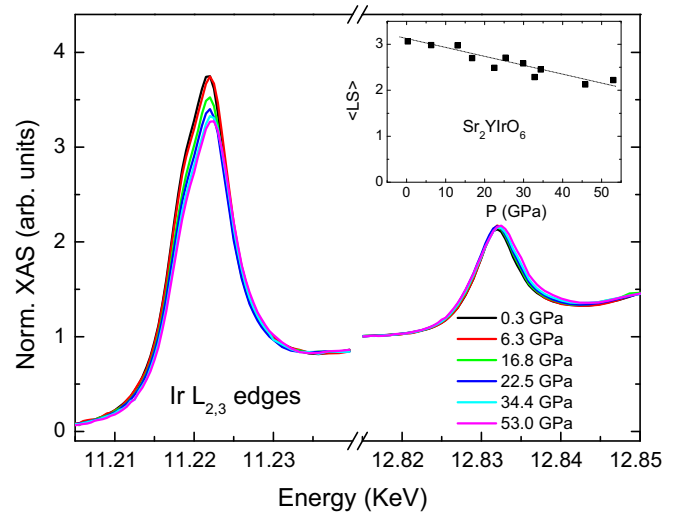


FIG. 10. XANES spectra recorded at room temperature at the Ir $L_{2,3}$ edges of Sr_2YIrO_6 as a function of pressure. The same evolution is observed at 10 K (not shown). The inset shows the $\langle \mathbf{L} \cdot \mathbf{S} \rangle$ as a function of applied pressure.

This implies a gradual decrease of the ground-state expectation value of the angular part of the spin-orbit coupling $\langle \mathbf{L} \cdot \mathbf{S} \rangle$, calculated via $BR = (2 + \langle \mathbf{L} \cdot \mathbf{S} \rangle / n_h) / (1 - \langle \mathbf{L} \cdot \mathbf{S} \rangle / n_h)$ [48], from ~ 3.1 down to ~ 2.2 ($\sim 0.5\%/GPa$). A 30% reduction is significant and may be indicative of an increasing bandwidth and/or an incipient mixing of $j = 1/2$ and $3/2$ subbands. Nevertheless, the $\langle \mathbf{L} \cdot \mathbf{S} \rangle$ values remain large, which indicates that the system still stays in the high SOC regime and is closer to the $J = 0$ state. Compared to this, the reduction of $\langle \mathbf{L} \cdot \mathbf{S} \rangle$ with Ca-doping is smaller: $\sim 2\%$ for $x = 0.4$.

As the pressure increases there is also a slight, gradual shift (~ 0.012 eV/GPa) of the Ir L_3 -edge XANES toward higher energies. As demonstrated by XMCD (see below), the spectral shift observed at the XANES is purely due to Ir-O bond length

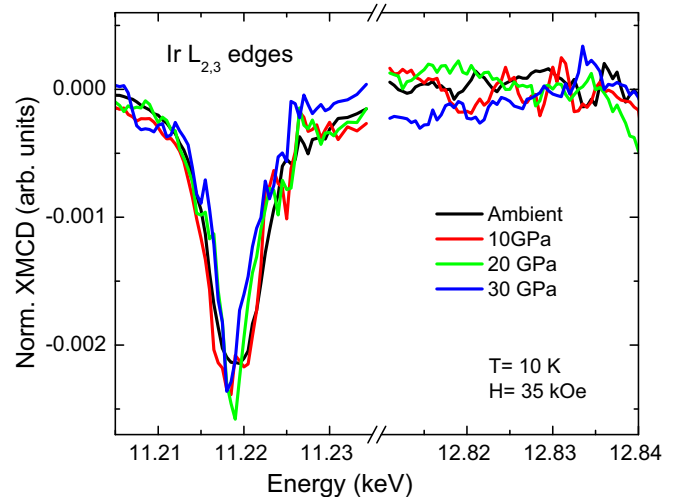


FIG. 11. XMCD spectra recorded at the Ir $L_{2,3}$ edges as a function of applied pressure. For the sake of clarity, the experimental data recorded under pressure have been (adjacent-averaging) smoothed.

contraction [49] and is not related to an evolution from Ir⁵⁺ to Ir⁶⁺.

Figure 11 shows the XMCD as a function of applied pressure. No spectral modification is observed as the pressure increases. This shows that no electron transfer from the Ir ion occurs. Indeed, the lack of electron transfer is not surprising in this system given the fully occupied electronic configuration of the different (Sr,O,Y) elements. More importantly, Fig. 11 demonstrates that the large structural modification observed by EXAFS spectroscopy does not cause any observable modification of the magnetic state.

V. DISCUSSION

Regarding the origin of the magnetism in these samples, the analysis of the ambient-pressure XMCD data reveals striking results. As seen in Fig. 7, the match between Sr_{1.6}Ca_{0.4}YIrO₆ and Sr₂ZnIrO₆ samples is quite remarkable, thus being strong evidence that the signal comes from Ir⁶⁺ for $x = 0.4$. This, in turn, indicates that (i) the Ir⁵⁺ ions do not have any significant contribution to the XMCD, even when they are the majority, and (ii) the XMCD of the Sr₂YIrO₆ sample does not rule out the presence of small amounts of Ir⁴⁺ ions. The stark difference between Sr_{1.6}Ca_{0.4}YIrO₆ and Sr₂YIrO₆ XMCD spectra reinforces this idea. Incidentally, in light of these results the conclusions regarding the Ir⁵⁺ iridates in Ref. [46] should be revisited.

Following this line of argument, the differences in the XMCD recorded for Sr_{1.6}Ca_{0.4}YIrO₆ and Sr₂YIrO₆ suggest an explanation in terms of unsystematic microstructural differences driven by the particular growth conditions. This could also explain the differences observed between the four samples in Fig. 5, as well as the dispersion in $M(H, T)$ found in the literature and why Fuchs *et al.* reported a major Ir⁶⁺ contribution in the nondistorted Ba₂YIrO₆ sample [18].

The presence of Ir⁶⁺ in Sr_{1.6}Ca_{0.4}YIrO₆ can result from cation vacancies or from partial substitution of Ir by Y ions or Y by Ca ions. In our Sr_{1.6}Ca_{0.4}YIrO₆, 11% of Ca at Y sites is found by XRD. On the other hand, the formation of Ir⁴⁺ ions in SYIO would be favored by both oxygen vacancies and partial substitution of Y by Ir atoms. Y/Ir antisite disorder would also favor Ir⁴⁺, locally. No evidence of off-stoichiometry is found in our SYIO. Similarly, in several works, the inclusion of off-stoichiometry on the refinements of XRD and neutron powder diffraction (NPD) data was reported not to lead to better fit results [11,13,14]. Dey *et al.* did not notice any change in the magnetic properties before and after annealing their Ba₂YIrO₆ sample [14], and Chen *et al.* found that their EDX measurements do not suggest any deviation of Ba, Sr, Y, and Ir from stoichiometry [26]. Nevertheless, it should be noticed that (i) there is limited accuracy in the occupancy factors of oxygen atoms from XRD measurements, and (ii) the amount of defects needed is very low. For instance, only 0.25% oxygen vacancies would result in 3% of Ir⁴⁺. Regarding the Y/Ir antisite, a 0.6% swap is obtained in SYIO.

Can the magnetism observed in Sr_{2-x}Ca_xYIrO₆ be assigned to the presence of a few percent ($\leq 3\%$ in the case of our SYIO) of isolated paramagnetic Ir⁴⁺ and/or Ir⁶⁺

centers? If we assume that this small number of *impurities* are randomly distributed through the sample, the existence of magnetic correlations is rather puzzling. If verified, this would imply that these centers can establish magnetic correlations at remarkably long distances. This would be quite a notable result. On the other hand, μ SR experiments evidence an inhomogeneous behavior with the presence of magnetic order in a $\sim 17\%$ fraction of the sample. In addition, the analysis of these data suggests a sizable Ir magnetic moment and the presence of magnetic correlations even at temperatures below 200 K. The behavior observed by μ SR is better explained in terms of small magnetic domains locally ordered, i.e., short-range order or short-range correlations.

These small domains could originate by the formation of antisite disordered regions. According to Chen *et al.* [26], the formation of magnetic moments would be favored in the Y/Ir antisite disordered clusters because of enhanced interactions due to increased orbital overlap and an increased number of orbitals mediating the interactions. In the case of SYIO, the level of Y/Ir antisite, 0.6%, is smaller than the $\sim 2.4\%$ needed to explain the $\sim 17\%$ volume fraction of magnetically ordered phase observed by μ SR. While the observed Y/Ir antisite certainly contributes to the formation of magnet clusters, additional mechanisms, which are unclear to date, must also be contributing. Besides, in perovskites with partial ordering, it is not unusual for the degree of antisite mixing to be sensitive to variations in synthesis conditions [50]. Regarding the Ca-doped samples, the enhanced magnetic response relative to SYIO that is observed in Figs. 6 and 5 can also be explained (and at least partially) in terms of antisite-induced magnetic clusters. As the doping level of Ca increases, an increasing part of it is incorporated at the Y sites. This implies an increasing formation of disordered regions containing Ir⁶⁺ ions that may interact magnetically (or even might polarize the Ir⁵⁺ ions around). Alternatively, Chaloupka *et al.* propose that light doping with d^5 ions ($J = 1/2$ states) could be another mechanism to create magnetic clusters. In particular, they found that the interaction between J excitons and doped carriers may convert the nonmagnetic parent into a ferromagnet [27]. Nevertheless, further work would still be needed to better clarify the role of Ir⁴⁺/Ir⁶⁺ ions in the formation and behavior of magnetic clusters.

With respect to the role of structure, as shown by XRD and EXAFS results, the structural modification caused by physical pressure is larger than that due to Ca-doping. In particular, the IrO₆ octahedron becomes smaller and more distorted applying hydrostatic pressure. Similarly, the Ir-O-Y angle undergoes a more drastic modification when physical pressure is applied. These structural changes could be expected to modify both the crystal field and the magnetic exchange. Despite that, the magnetism of the SYIO sample remains constant as hydrostatic pressure is applied, as clearly shown in Fig. 11. Therefore, it can be concluded that the magnetism of the Ir⁵⁺ ions in double perovskites cannot be tuned through small structural distortions. Neither volume contraction nor the structural distortions cause any change in the magnetic response. Similarly, it can be concluded that physical pressure does not affect either of the Ir⁴⁺ ions present in the SYIO sample.

On the other hand, the $J_{\text{eff}} = 1/2$ state of Ir^{4+} relies on a nearly cubic crystal field, and substantial distortions of the IrO_6 octahedron are expected to destroy the J_{eff} state, leading to a quenched orbital moment [51]. However, the exact relationship between noncubic distortions and the $J_{\text{eff}} = 1/2$ state is currently unknown. While even a small tetragonal distortion, as observed in Sr_2IrO_4 and $\text{Sr}_3\text{Ir}_2\text{O}_7$, can lead to some orbital mixing [52], a dominant $J_{\text{eff}} = 1/2$ character is preserved even within the distorted octahedra of the $A_2\text{IrO}_3$ ($A = \text{Li, Na, Cu}$) family [53,54]. Nevertheless, it is well established that, in transition-metal oxides, the local structure ~ 1 nm around a dopant can be highly distorted [41]. Thus, one could speculate that the quenched $\langle m_L \rangle$ seen in $\text{Sr}_{1.6}\text{Ca}_{0.4}\text{YIrO}_6$ occurs due to Ir^{4+} ions placed in highly distorted octahedra. The fact that the EXAFS does not see any distortion might simply be because it is difficult to distinguish the disordered octahedra (i.e., the EXAFS would not have enough resolution). However, while we cannot categorically dismiss such a scenario, we note that Ca-doping has a minor effect on $\langle \mathbf{L} \cdot \mathbf{S} \rangle$, which is difficult to reconcile with a quenched $\langle m_L \rangle$. Besides, the physical HP-XMCD results seem to disagree with this hypothesis and support the microstructural origin, as discussed above.

Finally, the possible emergence of excitonic magnetism ($J = 1$ exciton) induced by Ca-doping is discussed. According to our EXAFS results, the Ca-doping does not cause any measurable modification of the IrO_6 octahedra, but it increases the tilting of the Ir-O-Y angles. Therefore, we can reasonably assume that the spin-orbit-coupling (SOC), crystal electric field (CEF), on-site Coulomb interactions (U), and Hund's coupling (J_H) remain constant as the Ca-doping increases. The interatomic exchange, on the other hand, can be expected to decrease as a consequence of the larger Ir-O-Y tilting observed. Since the reduction of the interatomic exchange is a hindrance against the condensation of $J = 1$ triplon excitations, we can rule out that the enhanced magnetization signal in the doped samples is related to the onset of excitonic magnetism.

VI. CONCLUSIONS

Our XMCD data reveal that the magnetic signal comes from Ir^{6+} (Ir^{4+}) ions for $x = 0.4$ ($x = 0$). The Ir^{5+} ions do not have any significant contribution to the XMCD even when they are the majority. In addition, macroscopic magnetization, XMCD, and μSR experiments show that the magnetic response in $\text{Sr}_{2-x}\text{Ca}_x\text{YIrO}_6$ samples is rooted in the formation of magnetic clusters. The disparity found for different Ca-dopings indicates the crucial role of microstructural details (antisite disorder, and off-stoichiometry) in defining the overall magnetic response.

On the other hand, from the results obtained under physical pressure, it can be clearly concluded that the nonmagnetic state of the Ir^{5+} ions in these double perovskites is robust and not dependent on the structural details (Ir-O distances and Y-O-Ir angles). As a result, it cannot be tuned through small structural distortions. Neither volume contraction nor the structural distortions cause any change in the magnetic response.

ACKNOWLEDGMENTS

This work was partially supported by the Spanish MINECO projects MAT2014-54425-R and MAT2017-83468-R. E.A.-E. acknowledges the Spanish MINECO and the European Social Fund for a FPI (Formación de Personal Investigador, 2015) grant. C.A.E.Jr. is supported by FAPESP (Brazil) under Contract No. 2016/24137-3. This research used resources of the APS, a US Department of Energy (DOE) Office of Science User Facility operated for the DOE Office of Science by Argonne National Laboratory under Contract No. DE-AC02-06CH11357. We acknowledge the ESRF for provision of synchrotron radiation facilities. The XRD experiments were performed at BL04-MSPD beamline at ALBA Synchrotron with the collaboration of the ALBA staff. The authors would like to acknowledge the use of Servicio General de Apoyo a la Investigación-SAI, Universidad de Zaragoza.

-
- [1] B. J. Kim, H. Jin, S. J. Moon, J.-Y. Kim, B.-G. Park, C. S. Leem, J. Yu, T. W. Noh, C. Kim, S.-J. Oh *et al.*, *Phys. Rev. Lett.* **101**, 076402 (2008).
 - [2] A. Go, W. Witczak-Krempa, G. S. Jeon, K. Park, and Y. B. Kim, *Phys. Rev. Lett.* **109**, 066401 (2012).
 - [3] X. Wan, A. Vishwanath, and S. Y. Savrasov, *Phys. Rev. Lett.* **108**, 146601 (2012).
 - [4] M. Kargarian, J. Wen, and G. A. Fiete, *Phys. Rev. B* **83**, 165112 (2011).
 - [5] A. A. Burkov and L. Balents, *Phys. Rev. Lett.* **107**, 127205 (2011).
 - [6] W. Witczak-Krempa and Y. B. Kim, *Phys. Rev. B* **85**, 045124 (2012).
 - [7] X. Wan, A. M. Turner, A. Vishwanath, and S. Y. Savrasov, *Phys. Rev. B* **83**, 205101 (2011).
 - [8] W. Witczak-Krempa, G. Chen, Y. B. Kim, and L. Balents, *Annu. Rev. Condens. Matter Phys.* **5**, 57 (2014).
 - [9] M. Braden, G. Andre, S. Nakatsuji, and Y. Maeno, *Phys. Rev. B* **58**, 847 (1998).
 - [10] G. Cao, T. F. Qi, L. Li, J. Terzic, S. J. Yuan, L. E. DeLong, G. Murthy, and R. K. Kaul, *Phys. Rev. Lett.* **112**, 056402 (2014).
 - [11] J. Terzic, H. Zheng, F. Ye, H. D. Zhao, P. Schlottmann, L. E. DeLong, S. J. Yuan, and G. Cao, *Phys. Rev. B* **96**, 064436 (2017).
 - [12] B. F. Phelan, E. M. Seibel, D. Badoe, W. Xie, and R. Cava, *Solid State Commun.* **236**, 37 (2016).
 - [13] B. Ranjbar, E. Reynolds, P. Kayser, B. J. Kennedy, J. R. Hester, and J. A. Kimpton, *Inorg. Chem.* **54**, 10468 (2015).
 - [14] T. Dey, A. Maljuk, D. V. Efremov, O. Kataeva, S. Gass, C. G. F. Blum, F. Steckel, D. Gruner, T. Ritschel, A. U. B. Wolter *et al.*, *Phys. Rev. B* **93**, 014434 (2016).
 - [15] L. T. Corredor, G. Aslan-Cansever, M. Sturza, K. Manna, A. Maljuk, S. Gass, T. Dey, A. U. B. Wolter, O. Kataeva, A. Zimmermann *et al.*, *Phys. Rev. B* **95**, 064418 (2017).

- [16] K. K. Wolff, S. Agrestini, A. Tanaka, M. Jansen, and L. H. Tjeng, *Z. Anorg. Allg. Chem.* **643**, 2095 (2017).
- [17] M. Kusch, V. M. Katukuri, N. A. Bogdanov, B. Büchner, T. Dey, D. V. Efremov, J. E. Hamann-Borrero, B. H. Kim, M. Krisch, A. Maljuk *et al.*, *Phys. Rev. B* **97**, 064421 (2018).
- [18] S. Fuchs, T. Dey, G. Aslan-Cansever, A. Maljuk, S. Wurmehl, B. Büchner, and V. Kataev, *Phys. Rev. Lett.* **120**, 237204 (2018).
- [19] B. Yuan, J. P. Clancy, A. M. Cook, C. M. Thompson, J. Greedan, G. Cao, B. C. Jeon, T. W. Noh, M. H. Upton, D. Casa *et al.*, *Phys. Rev. B* **95**, 235114 (2017).
- [20] S. Bhowal, S. Baidya, I. Dasgupta, and T. Saha-Dasgupta, *Phys. Rev. B* **92**, 121113(R) (2015).
- [21] Q. Cui, J.-G. Cheng, W. Fan, A. E. Taylor, S. Calder, M. A. McGuire, J.-Q. Yan, D. Meyers, X. Li, Y. Q. Cai *et al.*, *Phys. Rev. Lett.* **117**, 176603 (2016).
- [22] G. Khaliullin, *Phys. Rev. Lett.* **111**, 197201 (2013).
- [23] O. N. Meetei, W. S. Cole, M. Randeria, and N. Trivedi, *Phys. Rev. B* **91**, 054412 (2015).
- [24] K. Pajskr, P. Novák, V. Pokorný, J. Koloren, R. Arita, and J. Kuneš, *Phys. Rev. B* **93**, 035129 (2016).
- [25] C. Svoboda, M. Randeria, and N. Trivedi, *Phys. Rev. B* **95**, 014409 (2017).
- [26] Q. Chen, C. Svoboda, Q. Zheng, B. C. Sales, D. G. Mandrus, H. D. Zhou, J.-S. Zhou, D. McComb, M. Randeria, N. Trivedi *et al.*, *Phys. Rev. B* **96**, 144423 (2017).
- [27] J. Chaloupka and G. Khaliullin, *Phys. Rev. Lett.* **116**, 017203 (2016).
- [28] F. Fauth, I. Peral, C. Popescu, and M. Knapp, *Powder Diffr.* **28**, S360 (2013).
- [29] J. Rodriguez-Carvajal, *Physica B* **192**, 55 (1993).
- [30] O. Mathon, A. Betheva, J. Borrel, D. Bugnazet, S. Gatla, R. Hino, I. Kantor, T. Mairs, M. Muñoz, S. Pasternak *et al.*, *J. Synch. Rad.* **22**, 1548 (2015).
- [31] S. Pascarelli, O. Mathon, T. Mairs, I. Kantor, G. Agostini, C. Strohmer, S. Pasternak, F. Perrin, G. Berruyer, P. Chappelet *et al.*, *J. Synch. Rad.* **23**, 353 (2016).
- [32] T. Irifune, A. Kurio, S. Sakamoto, T. Inoue, and H. Sumiya, *Nature* **421**, 599 (2003).
- [33] D. E. Sayers and B. Bunker, *X-Ray Absorption: Principles, Applications, Techniques of EXAFS, SEXAFS, and XANES* (Wiley, New York, 1988), Chap. 6.
- [34] M. Newville, *J. Synch. Rad.* **8**, 322 (2001).
- [35] B. Ravel and M. Newville, *J. Synch. Rad.* **12**, 537 (2005).
- [36] K. Hirano, K. Izumi, T. Ishikawa, S. Annaka, and S. Kikuta, *Jpn. J. Appl. Phys.* **30**, L407 (1991).
- [37] J. C. Lang and G. Srajer, *Rev. Sci. Instrum.* **66**, 1540 (1995).
- [38] M. Suzuki, N. Kawamura, M. Mizumaki, A. Urta, H. Maruyama, S. Goto, and T. Ishikawa, *Jpn. J. Appl. Phys.* **37**, L1488 (1998).
- [39] D. Haskel, Y. C. Tseng, N. M. Souza-Neto, J. C. Lang, S. Sinogeikin, Y. Mudryk, V. K. Pecharsky, and K. A. G. Jr., *High Press. Res.* **28**, 185 (2008).
- [40] See Supplemental Material at <http://link.aps.org/supplemental/10.1103/PhysRevB.101.014449> for further details on structural information.
- [41] D. Haskel, E. A. Stern, F. Dogan, and A. R. Moodenbaugh, *Phys. Rev. B* **61**, 7055 (2000).
- [42] D. Haskel, Ph.D. thesis, University of Washington, 1998.
- [43] B. T. Thole, P. Carra, F. Sette, and G. van der Laan, *Phys. Rev. Lett.* **68**, 1943 (1992).
- [44] P. Carra, B. T. Thole, M. Altarelli, and X. Wang, *Phys. Rev. Lett.* **70**, 694 (1993).
- [45] M. A. Laguna-Marco, D. Haskel, N. Souza-Neto, J. C. Lang, V. V. Krishnamurthy, S. Chikara, G. Cao, and M. van Veenendaal, *Phys. Rev. Lett.* **105**, 216407 (2010).
- [46] M. A. Laguna-Marco, P. Kayser, J. A. Alonso, M. J. Martinez-Lope, M. van Veenendaal, Y. Choi, and D. Haskel, *Phys. Rev. B* **91**, 214433 (2015).
- [47] K. Manna, R. Sarker, S. Fuchs, Y. A. Onyikienko, A. K. Bera, G. A. Cansever, S. Kamusella, A. Maljuk, C. G. F. Blum, L. T. Corredor *et al.*, *Phys. Rev. B* **94**, 144437 (2016).
- [48] G. van der Laan and B. T. Thole, *Phys. Rev. Lett.* **60**, 1977 (1988).
- [49] J. Chaboy, *J. Synch. Rad.* **16**, 533 (2009).
- [50] P. Woodward, R.-D. Hoffmann, and A. Sleight, *J. Mater. Res.* **9**, 2118 (1994).
- [51] S. Bhattacharjee, S.-S. Lee, and Y. B. Kim, *New J. Phys.* **14**, 073015 (2012).
- [52] D. Haskel, G. Fabbri, M. Zhernenkov, P. P. Kong, C. Q. Jin, G. Cao, and M. van Veenendaal, *Phys. Rev. Lett.* **109**, 027204 (2012).
- [53] H. Gretarsson, J. P. Clancy, X. Liu, J. P. Hill, E. Bozin, Y. Singh, S. Manni, P. Gegenwart, J. Kim, A. H. Said *et al.*, *Phys. Rev. Lett.* **110**, 076402 (2013).
- [54] E. M. Kenney, C. U. Segre, W. Lafargue-Dit-Hauret, O. I. Lebedev, M. Abramchuk, A. Berlie, S. P. Cottrell, G. Simutis, F. Bahrami, N. E. Mordvinova *et al.*, *Phys. Rev. B* **100**, 094418 (2019).